Transport Upscaling under Flow Heterogeneity and Matrix-Diffusion in Three-Dimensional Discrete Fracture Networks[1]

Jeffrey D. Hyman

Computational Earth Science (EES-16), Earth and Environmental Sciences Division, Los Alamos National Laboratory, Los Alamos New Mexico, USA

Marco Dentz

Spanish National Research Council (IDAEA-CSIC), Barcelona, Spain

---

Abstract

We investigate the combined effects of network scale flow variability and retention due to matrix-diffusion on the scaling behavior of transport through fractured media. Two of the principal mechanisms controlling the transport of solutes through fractured low-permeability media are broad distributions of flow velocities and retention times in the solid matrix. We study the relative impact of these two processes under different initial conditions using a set of three-dimensional discrete fracture network simulations. We use these simulations to develop and calibrate an upscaled continuous time random walk (CTRW) approach for advective transport based on an Ornstein-Uhlenbeck model for the particle velocities that accounts for the fracture-matrix coupling using a compound Poisson process. This CTRW model can be conditioned on the initial solute distribution and allows to observe late-time scaling behavior at distances beyond what is feasible to observe using high-fidelity direct numerical simulations. We determine that the initial distribution of particles leads to marked differences in the persistent long-term scale behavior in the solute travel time distributions, even those undergoing retention due to matrix diffusion through

[1]Hyman and Dentz, Adv. Water Resour. 155, 103994, https://doi.org/10.1016/j.advwatres.2021.103994

implementation and analysis of the model.

Keywords: fracture networks, matrix diffusion, solute transport, injection mode, continuous time random walk

---

1. Introduction

The transit time of solutes carried along by flows within low-permeability/low-porosity fractured media is determined by the interplay of multiple phenomena [1, 2, 3, 4, 5, 6, 7]. Two of the principal mechanisms that govern the behavior of solutes are the structure of heterogeneous fluid velocity field within the fracture network through which the solute advects [8, 9, 10, 11, 12, 13, 14, 15] and mass transfer between mobile and immobile zones, e.g., diffusion into and out of the rock matrix surrounding the fracture network [16, 17, 18, 19, 20, 21, 22, 23, 24]. The relative impact of these two mechanisms depends on various hydrological and geophysical conditions, including how solutes enter the fracture network and properties of the rock matrix [17, 25, 26]. In general, the initial distribution of a solute entering a domain can be described using one of two conceptualizations: resident-based and flux-weighted injection [27]. Physically, resident-based injection corresponds to a source that introduces a solute uniformly throughout an input area. For this reason, it is also referred to as uniform injection. This boundary condition can be achieved in experiments or simulations by injecting a constant amount of mass into all inflow channels. In the field, it could correspond to multiple leaking canisters within a buffer zone surrounding a subsurface waste repository. In contrast, flux-weighted injection corresponds to a solute released in proportion to the in-flowing volumetric flow rate at a location of insertion. This boundary condition can be achieved by maintaining a constant concentration at all inflow channels and would correspond to a miscible chemical released into a packed-off bore-hole connected to multiple hydraulically active fractures. These two injection modes are known to result in different transport behaviors through both fractured and heterogeneous porous media [28, 29, 30, 31, 32, 33, 34, 35, 36, 37, 38, 39]. The

initial condition determines what regions in the domain are sampled by the particles during a pre-asymptotic / non-ergodic period. When particles enter the domain according to flux-weighting under ergodic conditions, the distribution of Lagrangian velocities sampled at equal distances along a pathline is stationary and can be related directly to the Eulerian velocity PDF through flux-weighting [40, 41, 35, 42]. In contrast, particles sample the *unweighted* Eulerian velocity distribution along the inlet plane under resident initial conditions. As particles move through the system, they channelize into regions of higher velocity and evolve into the steady-state Lagrangian distribution [34], i.e., the velocity PDF is not initially stationary. The particles injected under resident conditions sample more low velocities than their flux-weighted counterparts, and in turn, lower decay exponents in the advective travel time distributions are commonly observed [29, 35, 36, 34].

While these studies concerning the influence of particle injection mode have advanced our understanding of the impact of initial positions on transport, little is comparatively understood about the combined effects of injection mode and matrix diffusion. Field and laboratory experiments, as well as numerical simulations, have shown that solutes undergoing matrix-diffusion exhibit power-law scaling in the tails of the travel time distribution [16, 43, 44, 20, 21, 22, 23, 24]. In the classical model of matrix diffusion, this power-law tail decays with an exponent of -3/2 [22, 45, 46]. However, there are tracer tests in fractured rock that exhibit breakthrough curves where the exponent deviates from this classical prediction [20, 24, 16]. A number of theories and interpretations have been proposed to explain these differences [47, 17, 21, 48, 49]. A recent work [21] showed that under particular conditions, the interplay between advection and matrix-diffusion could lead to power-law tailing behavior with exponents deviating from the classically predicted -3/2 if the advective travel time distribution decays sufficiently slowly. Moreover, it was found [21, 50] that the influence of matrix diffusion manifests in breakthrough curves depending on the scale of observation. At short distances, there is a pre-asymptotic time regime that is fully determined by advective heterogeneity, while at longer times, there is an

asymptotic regime that shows the signatures of matrix diffusion.

We characterize the relative impact of flow heterogeneity and matrix diffusion at different initial conditions on long-term transport behavior in fracture networks using a combination of high-fidelity simulations and upscaled transport models. For the high-fidelity models, we perform a series of flow and transport simulations in a semi-generic three-dimensional discrete fracture network (DFN) at the kilometer scale. DFN models are a simulation methodology to model flow and transport through a fractured medium where fractures are explicitly represented, cf. Berre et al. [51] for a review of modern approaches for the simulation flow and transport in fractured media. We represent solute transport as a plume of passive tracer particles to characterize the influence of both uniform and flux-weighted injection modes. We observe particle attributes, e.g., travel time and path line distance, at uniformly spaced control planes throughout the network. We observe purely advective transport as well as that retarded by matrix diffusion. This particle-based methodology readily allows for the inclusion of matrix diffusion into a DFN model using a time-domain random walk (TDRW) where the total travel time of a particle is a combination of the time advecting through the in-fracture flow field and time spent diffusing into and out of the matrix [52, 53, 21, 54].

The computational expense of running DFN simulators limits their usage to study transport at large scales, which is required to observe the relative impact of injection mode and matrix diffusion. This limitation has prompted the use of upscaled transport models such as the continuous-time random walk (CTRW) and fractional-order transport models [55, 56, 57, 58, 59] to study flow and transport in fractured media. To this end, we develop a CTRW model for advective transport based on an Ornstein-Uhlenbeck model for the particle velocities and the fracture-matrix coupling based on a compound Poisson process. We calibrate the model using the DFN simulations and then provide observations of transport behavior beyond what is observable using the high-fidelity simulations. Additionally, we use this model to derive the expected scalings of the breakthrough curves, which we compare to the CTRW observations. Through

implementation and analysis of the models, we determine that the initial distribution of particles leads to marked differences in the persistent long-term scale behavior undergoing retention due to matrix diffusion.

2. Solute Transport

We represent solute transport using a plume of indivisible nonreactive particles, i.e., using a Lagrangian approach. This section describes how the initial positions of particles are determined and then their movement through the fluid velocity field within the fracture network.

2.1. Initial Positions

There are multiple methods to determine the distribution of particles under resident/uniform and flux-weighted conditions. In one numerical method, all particles are assigned the same mass, and the distribution of their locations distinguishes injection mode. Let M denote the total mass of a solute represented by N individual particles. Let $\{\mathbf{x}_0\}$ denote the set of initial positions along fractures intersecting with the inlet plane denoted Ω_0. We use equi-spacing (uniform distance) between points in $\{\mathbf{x}_0\}$ along the fracture intersections. The value of this distance depends on the total intersection length of fractures along Ω_0 and N, $\delta l = \Omega_0/N$. To represent resident injection, the same number of particles n are placed at every point in $\{\mathbf{x}_0\}$

$$n(\mathbf{x}_0) = \left\lceil \frac{M}{N} \right\rceil \qquad \forall \qquad \mathbf{x}_0 \in \{\mathbf{x}_0\} \ . \tag{1}$$

For flux-weighting, we also need to consider the volumetric flow rate across the entire inflow face and at every point in $\{\mathbf{x}_0\}$. The total volumetric flow rate $\bar{Q}$ along Ω_0 is defined as

$$\bar{Q} = \int_{\Omega_0} d\mathbf{x}_0 Q(\mathbf{x}_0) \ . \tag{2}$$

where $Q(\mathbf{x}_0)$ is the volumetric flow rate at $\mathbf{x}_0$. Then the number of particles placed at $\mathbf{x}_0$ is proportional to the volumetric flow rate at that point

$$n(\mathbf{x}_0) = \left\lceil \frac{M}{N} \frac{Q(\mathbf{x}_0)}{\bar{Q}} \right\rceil \ . \tag{3}$$

In an alternative numerical method, particles are assigned different portions of the total mass, but same number of particles are assigned to every point in $\{\mathbf{x}_0\}$. To represent resident injection, the mass of a single particle $m(\mathbf{x}_0)$ placed at point in $\{\mathbf{x}_0\}$ is

$$m(\mathbf{x}_0) = \frac{M}{N} \qquad \forall \qquad \mathbf{x}_0 \in \{\mathbf{x}_0\} \tag{4}$$

and for flux-weighted

$$m(\mathbf{x}_0) = \frac{M}{N} \frac{Q(\mathbf{x}_0)}{\bar{Q}} \tag{5}$$

By comparison, the two methods resident injection ((1) and (4)) are clearly equivalent. For flux-weighting, comparison of (3) and (5) indicates that the methods become equivalent as the number of particles or initial positions becomes sufficiently large. The primary advantage of the second method is that the number of initial positions can be substantially larger than when using the first method for the same number of particles, which can facilitate improved sampling of the velocity field with fewer particles. We adopt the second method in our simulations.

2.2. Particle Transport

We consider first purely advective transport of particles that originate from the position $\mathbf{x}_0$ in the inlet plane Ω_0 located at $x = 0$, which is perpendicular to the mean flow direction. The particle position $\mathbf{x}(t)$ evolves according to the advection equation

$$\frac{d\mathbf{x}(t)}{dt} = \mathbf{u}[\mathbf{x}(t)], \qquad \mathbf{x}(t=0) = \mathbf{x}_0. \tag{6}$$

The advective transport problem can be formulated equivalently in terms of the distance $s(t)$ traveled by a particle along a streamline. The length $s(t)$ of the trajectory at a time t is given by

$$\frac{ds(t)}{dt} = u[\mathbf{x}(t)]. \tag{7}$$

where we defined the Lagrangian velocity magnitude $u[\mathbf{x}(t)] = |\mathbf{u}[\mathbf{x}(t)]|$. As mentioned above, the length of the pathline, s, is used to parameterize the

spatial and temporal coordinates of the particle. Thus, changing variables according to $dt \rightarrow u[\mathbf{x}(s)]ds$, we obtain for the space-time particle trajectory in terms of s

$$\frac{d\mathbf{x}(s)}{ds} = \frac{\mathbf{v}(s)}{v(s)} \qquad \frac{dt(s)}{ds} = \frac{1}{v(s)} \tag{8}$$

where we defined the space-Lagrangian velocity $\mathbf{v}(s) = \mathbf{u}[\mathbf{x}(s)]$ and its magnitude $v(s) = |\mathbf{v}(s)|$. When particles arrive at a fracture intersections, we assume the flow is diffusion dominated and the probability to enter an outgoing fracture is weighted by the outgoing volumetric flow rate, i.e., a complete mixing rule is applied [60, 61, 62, 63, 64, 65]. Note that this stochastic method at intersections leads to dispersion of particles with the same initial position, which would otherwise follow the same deterministic pathline through the network. We do not consider molecular diffusion in these simulations.

There are a variety of mathematical formulations to include the effects of matrix diffusion into transport models, cf. Carrera et al. [17] for a review. The general idea is that a source/sink term representing mass diffusing into and out of the matrix is included into the solute transport equation. A key difference between the proposed models is the form of the source/sink term representing matrix diffusion [66]. We account for particles diffusing in and out of the matrix using the time domain random walk (TDRW) approach detailed in Delay and Bodin [53], which is agnostic to the initial distribution of mass into the domain. Details of the specific implementation are given in Appendix A. We consider the duration a particle spends within a fracture media to be the sum of the times spent advecting through the fracture network and the times retained within the surrounding rock matrix.

3. Upscaled Transport Model

In this section, we present the CTRW approach for advective transport that is based on an Ornstein-Uhlenbeck model for the particle speeds [67, 68, 69]. The fracture-matrix coupling is quantified by a compound Poisson process. Furthermore, we derive the expected scalings of the breakthrough curves.

3.1. Advective transport: Ornstein-Uhlenbeck model for velocity transitions

We model particle motion by a CTRW combined with an Ornstein-Uhlenbeck process for the normal scores of particle velocity as described in the following. We assume that the series $v(s)$ of equidistantly sampled particle speeds (see, Eq. 8) form a stationary Markov process with the limit distribution $p_s(v)$. Under ergodic conditions, this means for a sufficiently large injection volume and flow domain, the steady space Lagrangian PDF $p_s(v)$ and the Eulerian velocity PDFs are related through flux-weighting [40, 41, 35],

$$p_s(v) = \frac{v p_e(v)}{\langle v_e \rangle}. \tag{9}$$

Stationary Markov models for equidistantly sampled particle speeds have been used for the prediction of transport in fractured and [70, 14] and porous media [71, 72, 40, 68, 69]. Stationarity is assumed to hold also for the normal scores $w(s)$ of particle speeds $v(s)$, which are defined by

$$w = \Phi^{-1}[P_s(v)], \qquad P_s(v) = \int_0^v dv' p_s(v'), \tag{10}$$

where $\Phi(w)$ is the cumulative unit Gaussian distribution and $P_s(v)$ is the cumulative distribution of particle speeds. Based on the Doob theorem [73] we thus model the evolution of the normal $w(s)$ with distance s along the streamline by the Ornstein-Uhlenbeck process

$$\frac{dw(s)}{ds} = -\gamma w(s) + \sqrt{2\gamma}\xi(s), \tag{11}$$

where $\xi(s)$ is a Gaussian white noise characterized by zero mean and $\langle \xi(s)\xi(s') \rangle = \delta(s - s')$. The relaxation parameter $\gamma = \ell_c^{-1}$ is the inverse of the correlation length scale ℓ_c. The initial values $w_0 = w(s = 0)$ are given in terms of the initial speeds $v_0 = v(s = 0)$ by (10). The distribution of initial velocities is denoted by $p_0(v)$. It varies depending on the injection mode, see Section 2.1. The particle speed $v(s)$ is given by $w(s)$ by inverting (10) as

$$v(s) = P_v^{-1}(\Phi[w(s)]) \tag{12}$$

The Ornstein-Uhlenbeck model describes the stochastic evolution of $v(s)$ from an arbitrary initial distribution $p_0(v)$. It is a stochastic model for the sequence of particle speeds along trajectories. Note that this Markov model for the particle speeds does not require detailed knowledge of the high-fidelity trajectories, but only needs as an input the point distribution $p_s(v)$ of particle speeds, which can be related to the flow speeds through equation (9), and the characteristic relaxation scale ℓ_c.

Particle motion along a streamline is described here by its advective travel time $t_a(s)$, which satisfies according to (8)

$$\frac{dt_a(s)}{ds} = \frac{1}{v(s)}. \tag{13}$$

where $v(s)$ is obtained from the Ornstein-Uhlenbeck process described above. The CTRW quantifies the travel time $t(s)$ up to a distance s along streamlines. The linear distance x between the inlet and control planes and the distance s along the tortuous streamlines are related through tortuosity χ as $x = s/\chi$. Tortuosity is discussed in detail in Section 4.3.4. In this sense, this approach models the particle trajectories projected onto the mean flow direction, this means as one-dimensional objects. The distribution $f_v(t, x)$ of advective travel times at a distance x from the inlet boundary is given by

$$f_a(t, x) = \langle \delta[t - t_a(x\chi)] \rangle. \tag{14}$$

3.2. Matrix Diffusion: Compound Poisson process for fracture-matrix mass transfer

We couple the CTRW model discussed in the previous section with diffusive mass transfer between fracture and matrix. The series of residence or trapping times in the matrix is modeled as a compound Poisson process [74, 75, 50, 76]. This assumes that trapping occurs at a constant rate γ, which is related to the diffusion time over the fracture cross section. The particle time $t(s)$ at a given distance s along the path is then given by

$$t(s) = t_a(s) + \tau_c[t_a(s)], \qquad \tau_c(t) = \sum_{k=1}^{n_t} \eta_i. \tag{15}$$

The residence times η_i in the matrix are distributed according to $\psi_f(t)$, which is specified below. The number n_t of trapping events up to time t is Poisson-distributed,

$$p_n(t) = \frac{(\gamma t)^n \exp(-\gamma t)}{n!}. \tag{16}$$

The distribution $\psi_c(t'|t) = \langle \delta[t' - \tau_c(t)] \rangle$ of $\tau_c(t)$ is given in Laplace space by

$$\psi_c^*(\lambda) = \exp\left(-\gamma t \left[1 - \psi_f^*(\lambda)\right] - \lambda t\right). \tag{17}$$

We consider a semi-infinite matrix. Thus, the trapping time distribution is given by the inverse Gaussian distribution

$$\psi_f(t) = \frac{\epsilon \exp(-\epsilon^2/4D_m t)}{\sqrt{4D_m t^3}}, \tag{18}$$

where D_m is the diffusion coefficient in the matrix. The trapping or residence time distribution is equivalent to the return time distribution to the boundary. The microscopic distance ϵ from the interface regularizes the return time distribution, which otherwise is not defined in the continuum [77, 78]. The regularization implies that $\psi_f(t)$ decays exponentially fast for times smaller than ϵ^2/D_m. At times $t \gg \epsilon^2/D_m$, it behaves as a power law $\sim t^{-3/2}$. Finiteness of the matrix implies a long time cut off at $\tau_D = {\ell_m}^2/D_m$, where ℓ_m is a characteristic matrix block scale. We assume here that τ_D is much larger than the observation time scale.

The trapping rate is given in terms of the effective fracture aperture b_e, porosity ϕ and the diffusion coefficient D_m as

$$\gamma = \frac{2\phi D_m}{\epsilon b_e}, \tag{19}$$

as detailed in Appendix B.

The distribution $f(t, x)$ of arrival times at distance $x = s/\chi$ from the inlet boundary is given in analogy to (14) by

$$f(t, x) = \delta[t - t(x\chi)]. \tag{20}$$

It is related to the travel time distribution $f_a(t,x)$ by

$$f(t,x) = \int_0^t dt' f_a(t',x)\psi_c(t-t'|t'), \tag{21}$$

This equation reads as follows. The probability for a particle arrival at time t is given by the probability that the particle travels to distance x in time t' times the probability that the compound trapping time is $t-t'$.

3.3. Scaling of breakthrough curves

In order to derive asymptotic expressions for the breakthrough curve scaling at a control plane at x, we coarse grain the velocity process on the correlation length ℓ_c, this means the particle speed is set constant over the distance ℓ_c, and sampled randomly according to $p_s(v)$ after the distance ℓ_c. This simplifies the time process (15) according to

$$t_{n+1} = \tau_n + \tau_c(\tau_n), \qquad \tau_n = \frac{\ell_c}{v_n}. \tag{22}$$

The distribution $\psi(t)$ of the combined advective transition and residence times over the distance ℓ_c is given in Laplace space by

$$\psi^*(\lambda) = \psi_a^*(\lambda + \gamma[1-\psi_f^*(\lambda)])^n, \tag{23}$$

where $\psi_a(t)$ is the steady state distribution of advective travel times. It is given in terms of the velocity distribution $p_s(v)$ as

$$\psi_a(t) = \frac{\ell_c}{t^2} p_s(\ell_c/t). \tag{24}$$

The transition time distribution for the first step of distance ℓ_c is accordingly given in terms of the initial velocity distribution $p_0(v)$ as

$$\psi_0(t) = \frac{\ell_c}{t^2} p_0(\ell_c/t). \tag{25}$$

Note that it is through $\psi_0(t)$ and $p_0(v)$ that the model includes the injection mode of the particles.

In this coarse grained picture, the breakthrough curve $f(t,x)$ is given by the n-fold self-convolution of the transition time distribution $\psi(t)$, which reads in Laplace space as

$$f^*(\lambda,x) = \psi_0^*(\lambda+\gamma[1-\psi_f^*(\lambda)])\psi_a^*(\lambda+\gamma[1-\psi_f^*(\lambda)])^{n_c-1}, \tag{26}$$

where $n_c = x\chi/\ell_c$. We note that the transition time distribution here behaves as $\psi_a(t) \propto t^{-1-\beta}$ with $1 < \beta < 2$, while the initial velocity distribution may scale as $\psi_0(t) \propto t^{-1-\alpha}$ with $0 < \alpha < 2$. Note that the exponent β in the steady state transition time distribution cannot be smaller than 1 because it is derived from the flux-weighted speed distribution $p_s(v) \sim v^{\beta-1}$. If the Eulerian speed distribution $p_e(v) \sim v^{\alpha-1}$ with $\alpha > 0$ at v smaller than some characteristic velocity v_0, it follows that $p_s(v) \sim v^{\beta-1}$ with $\beta = 1+\alpha > 1$.

The behavior of the breakthrough curves is determined by two relevant times scales. The scale $\bar{t}_c = x_c/\bar{u}$ measures the time for purely advective motion over the distance between the inlet and control planes. The time scale $\tau_\gamma = \gamma^{-1}$ is the average time a particle is mobile and the time scale $\tau_e = \gamma^2\epsilon^2/D$ denotes the time at which particles have spent the same amount of time in the fracture and in the matrix [50]. This means, for times $t < \tau_e$ advection in the network dominates and for $t > \tau_e$ retention in the matrix is the dominant process.

We first consider the case of a flux-weighted injection such that $\psi_0(t)$ behaves approximately as $\psi_a(t)$. For $\bar{t}_c < t < \tau_e$, the breakthrough curve is expected to scale as $f(t) \sim t^{-1-\beta}$ because transport is dominated by the network-scale advective heterogeneity because particles are mostly mobile and transport is dominated by advection in the network. For $t > \tau_e$, the matrix is activated as a retention mechanism and the breakthrough curves behaves according to the characteristic $f(t) \sim t^{-3/2}$ scaling.

Secondly, we consider the case of a uniform injection characterized by $\psi_0(t) \sim t^{-1-\alpha}$ with $0 < \alpha < 1$ while $\psi_a(t) \sim t^{-2-\alpha}$. As in the previous case, for $\bar{t}_c \ll t \ll \tau_e$, advection dominates and the breakthrough curve scales as $f(t) \sim t^{-1-\alpha}$. However, for $t \gg \tau_e$ the behavior of the breakthrough curves is affected by retention in the matrix and retention at the source zone due to slow advection.

This gives the breakthrough curve scaling $f(t) \sim t^{-1-\alpha/2}$. The derivations of these scaling behaviors are detailed in Appendix C.

4. DFN Flow and Transport Simulations

We perform a set of high-fidelity three-dimensional discrete fracture network (DFN) simulations using DFNWORKS [79] to determine the solute breakthrough curves, tortuosity of particle paths, and distributions of flow and particle speeds. We record both the advective breakthrough curves and breakthrough curves of particles undergoing advection and matrix diffusion at uniformly spaced control planes in the domain that are perpendicular to the primary direction of flow. We represent solute transport passing through the network using a plume of particles. We consider both uniform and flux-weighted injection modes for the initial positions of particles. We then observe attributes that are input parameters for the CTRW model: distribution of particle speeds, correlation length, and tortuosity. These parameters can in principle be obtained from non-Lagrangian observations [42, 12], see also Section 4.2. Here, we calibrate the CTRW model in terms of the Lagrangian observations, and use it for the characterization and prediction of the combined effect of network scale flow heterogeneity and matrix diffusion on solute transport beyond what is possible using the DFN model.

4.1. Discrete Fracture Network Model

We perform flow and transport simulations in a semi-generic DFN composed of a single family of disc-shaped fractures within a cubic domain with sides of length one kilometer. Fracture radii r are sampled from truncated power law distribution with exponent $\alpha = 2.6$ and upper and lower cutoffs ($r_u = 1000$ m ; $r_0 = 10$ m) with PDF $p_r(r)$ for the radius

$$p_r(r) = \frac{\alpha}{r_0} \frac{(r/r_0)^{-1-\alpha}}{1-(r_u/r_0)^{-\alpha}}. \tag{27}$$

Fractures in geological media are commonly observed to have length distributions that appear to follow a powerlaw distribution [2]. Fracture centers are

uniformly distributed throughout the domain. Fracture orientations are sampled from a Von-Mises Fisher distribution with intensity parameter $\kappa \approx 0$ and mean normal vector of $(0, 0, 1)$ using the method provided by [80]. This method results in normal vectors with a uniform covering of the unit sphere, which mimics disordered fractures networks composed of many families [81, 82]. There are 7055 fractures in the domain, which corresponds to a dimensionless density of 14 using the definition provided by [83], which indicates that the domain is 14 times denser than the critical percolation density value [84, 85, 86, 87]. The computational mesh of the DFN contains 11,368,981 nodes and 23,089,485 triangles. The mesh has been optionally refined near intersections to ensure that gradients in the pressure field, which are higher in these regions, are properly resolved [88]. The hydraulic aperture of the fractures b is positively correlated to the radii via a powerlaw relationship $b = 5.0 \times 10^{-4}\sqrt{r}$ and fracture permeability is determined by the cubic law [89]. Although it is possible to include in-fracture aperture variations into three-dimensional DFN simulation [9, 90, 91], we do not do so here. Our focus is on the interplay of injection mode, advective transport, and matrix diffusion rather than sub-fracture scale variability.

Flow in the fracture network is modeled using the Reynolds equation [92]. Flow through the network is created by applying a pressure difference of 4 kPa (1m/m gradient) across the domain aligned with the x-axis. This pressure difference allows to observes the effects of both advection and matrix diffusion within this domain and for selected matrix properties, but is not meant to represent a particular field site. No flow boundary conditions are applied along lateral boundaries. We use the methods of Makedonska et al. [93] and Painter et al. [94] to reconstruct Eulerian velocity field $\mathbf{u}(\mathbf{x})$ within each DFN. Figure 1 is an image of the network where fractures planes are colored by the logarithm (base 10) of the velocity magnitude divided by the mean velocity magnitude ($v_m = 2.72 \cdot 10^{-7}$ m/s). There are large contrasts in velocity values between fractures and smaller variations within the fractures. Larger fractures are better connected and more flow passes through them. Additionally, the positive correlation between hydraulic aperture and fracture size results in lower resistance

to flow within bigger fractures.

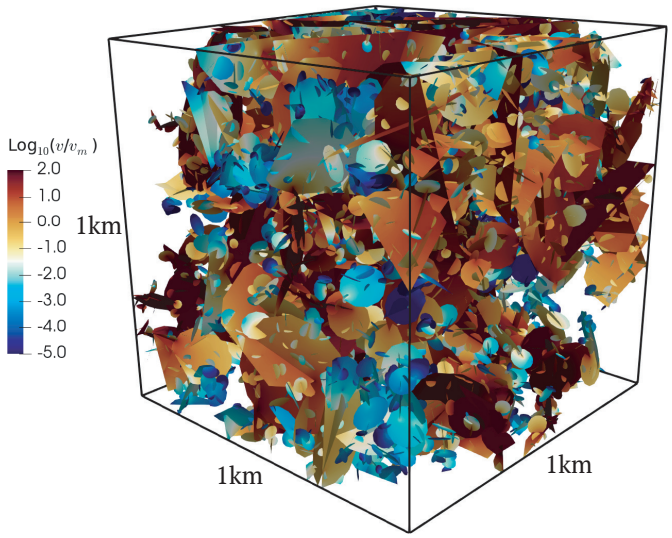

Figure 1: Discrete fracture network composed of 7055 disc-shaped fractures whose radii follow a powerlaw distribution. Colors denote the base ten logarithm of velocity magnitude divided by the mean velocity magnitude ($\log_{10}(v/v_m)$ where $v_m = 2.72 \cdot 10^{-7}$ [m/s]). There are large contrasts in velocity values between fractures and smaller variations within the fractures.

4.2. Velocity Distributions

The PDFs of Eulerian velocity magnitude (speed) are directly obtained from the reconstructed $|\mathbf{u}(\mathbf{x})|$ velocity field and the Lagrangian PDFs are obtained using the particle tracking methods described above. Figure 2 shows the Eulerian, flux-weighted Eulerian, and the space Lagrangian velocity PDFs as well as the space Lagrangian velocity PDF at the injection plane for the three fracture networks under consideration. Under ergodic conditions and for a sufficiently large injection volume and flow domain, the steady space Lagrangian PDF $p_s(v)$ and the Eulerian velocity PDFs are related through flux-weighting as previous discussed, cf. (9). In the samples shown here, we see good agreement between the steady s-Lagrangian PDF and flux-weighted PDF at high velocities, and the two deviate from one another at low velocity values. Nonetheless, there is good

agreement over five orders of magnitude. Also, the inlet velocity distribution appears to be representative of the full Eulerian PDF. The right panel shows the corresponding transition time distributions by directly inverting the velocity PDFs. The solid black lines denote the power-law scalings as $t^{-1-\beta}$ with $\beta = 0.2$, 1.2, 0.7, and 1.7. The high probability of low flow speeds translates into power-law tails in the transition time PDF. As we have seen in Section 3.3, power-law tails in $\psi(t)$ gives rise to intriguing non-Fickian behaviors in the solute breakthrough curves, which are discussed in detail in Section 5. We conjecture that the behaviors of the distribution of flow speeds and corresponding transition times can be related to network properties such as connectivity and aperture distribution, which, however, needs to be probed in further studies.

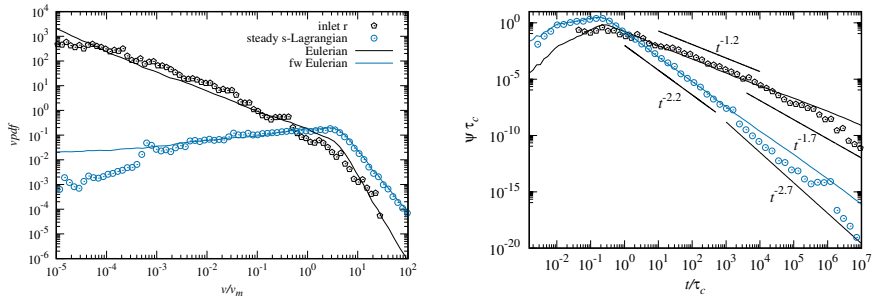

Figure 2: Left panel: (circles) steady s-Lagrangian velocity PDF, (pentagons) velocity PDF at inlet plane. The solid lines show the Eulerian speed PDF and the flux-weighted Eulerian speed PDF. Right panel: Corresponding transition time distributions. The solid black lines denote the power-law scalings as $t^{-1-\beta}$ with $\beta = 0.2$, 1.2, 0.7, and 1.7

4.3. Lagrangian transport attributes

A set of one-hundred thousand particles denoted Ω_a are tracked through the network. Increasing the number of particles beyond these counts did not influence observed quantities. We observe particle attributes at uniformly spaced control planes that are perpendicular to the primary direction of flow placed at 250, 500, 750, and 1000 meters from the inlet.

4.3.1. Breakthrough Curves

The first arrival time $\tau(x_1, \mathbf{x}_0)$ of a particle starting at $\mathbf{x}_0$ to reach a control plane located at x is given by

$$\tau(x_1, \mathbf{x}_0) = t[s|x_1(s) \geq x_1, \mathbf{x}_0], \tag{28}$$

where s is the pathline distance along the trajectory and x_1 corresponds to the first spatial component of the position vector. The mass represented by each particle $m(\mathbf{x}_0)$ and $\tau(x_1, \mathbf{x}_0)$ are combined to determine the solute mass flux $f(t, x)$ that has broken through a control plane at $x = x_1$ at a time t,

$$f(t, x_1) = \frac{1}{M} \int_{\Omega_a} d\mathbf{x}_0 m(\mathbf{x}_0) \delta[\tau(x_1, \mathbf{x}_0) - t], \tag{29}$$

where, $\delta(t)$ is the Dirac delta function. We refer to (29) as the breakthrough curve. We use (29) for both purely advective and advection/matrix diffusion travel times. In the latter case, the diffusion coefficient in the matrix is set to $D_m = 10^{-13}$ m^2/s and the porosity $\phi = 5 \times 10^{-2}$. These values are selected to allow to study both the effects of advection and matrix diffusion for this network and flow field, but not meant to represent a particular field site although they do fall within physically reasonable range of values for low permeability rocks [26].

4.3.2. Equivalent Aperture

The method implemented to account for matrix diffusion in DFNWORKS allows for hydraulic apertures to vary between fractures [21]. However, the presented upscaled transport model requires a single equivalent/effective aperture, which can be obtained by combining the advective travel time (28) with the Lagrangian retention parameter defined in Cvetkovic et al. [8],

$$\int_0^s \frac{2ds}{b(s)v'(s)} \ . \tag{30}$$

Dividing twice the advective travel time by (30) provides an integrated value for the resistance along a pathline and an effective aperture value b_{eff} [95]. We observed an average value of $b_{eff} = 0.0048$ m for flux-weighted and $b_{eff} = 0.0041$ m for resident injection at the outlet plane. In Appendix D, we compare

the DFN BTCs including matrix diffusion using the actual fracture hydraulic apertures that vary between fractures and the effective hydraulic apertures that show good agreement between the two methods.

4.3.3. Correlation Length

The autocorrelation of Lagrangian velocities is determined using the magnitude of particle velocities sampled equidistantly along pathlines:

$$C_{vv}(s) = \frac{1}{V_0} \int\limits_{\Omega_a} d\mathbf{x}_0 \int\limits_0^\infty ds' \frac{v_s'(s') v_s'(s'+s)}{\sigma_{vv}^2}, \tag{31}$$

where σ_{vv}^2 is the velocity variance and $v_s'(s)$ the fluctuation about the mean. The correlation distance ℓ_c is when fluctuations anticorrelate, which we take at the first zero crossing of (31). For resident injection $\ell_c = 221$ m and for flux-weighted injection $\ell_c = 204$ m. Note that C_{vv} is a purely advective quantity.

4.3.4. Tortuosity

We focus on a flow-dependent geometric tortuosity, as it is naturally compatible with Lagrangian observations; other tortuosity definitions can be found in [96]. Let $s(x_i, \mathbf{x}_0)$ be the total pathline distance of a particle upon its first crossing of a control plane at $x = x_i$. Then the tortuosity of the pathline defined

$$\chi(x_i) = \frac{s_i(\mathbf{x}_0)}{x_i}. \tag{32}$$

We take the average of χ over Ω_a. Under ergodic conditions, this means here at a linear distance $x_1 \gg \ell_c$ much larger than the characteristic fracture length, the tortuosity is given by [97]

$$\chi_\infty = \lim_{x_1 \to \infty} \chi(x_1) = \frac{\langle v_e \rangle}{\langle u_1 \rangle}. \tag{33}$$

The asymptotic tortuosity for this network is $\chi_\infty = 2.54$ due to higher number of relatively short fractures, which induces a high tortuosity in the particle path. Note that the asymptotic tortuosity does not depend on the particle injection mode. At finite distances, however, the tortuosity depends on the injection mode

and on the local fracture geometry. For resident injection, $\chi = 2.18$ (250m), 2.63 (500m), 2.78 (750m), and 2.55 (1000m). For flux-weighted $\chi = 1.62$ (250m), 2.11 (500m), 2.63 (750m), and 2.50 (1000m). The observed values of tortuosity do not fully stabilize at χ_∞, but the observed values at 1000 meters are close to these asymptotic value. The values of flux-weighted particles are always less than those observed for resident injection. Note that χ is a purely advective quantity.

5. Results

In this section, we discuss the behavior of solute breakthrough curves at different control planes. We consider two different injection conditions, uniform and flux-weighted, as discussed above. We first discuss the case of advective transport, and compare the DFN simulations with the CTRW model. Then we consider advective transport under matrix diffusion again for the two different injection conditions, and again compare the DFN simulations with the CTRW model. In the following, the breakthrough curves for the uniform injection are marked by blue, the ones for the flux-weighted injection by black lines or symbols.

5.1. Advective transport

Figure 3 shows solute breakthrough curves at different control planes for uniform and flux-weighted initial conditions. The symbols and lines denote the results from the direct numerical simulation and the CTRW model, respectively. We observe a stronger tailing for the uniform than for the flux-weighted injection at all control planes. This is due the fact that the uniform injection emphasizes the low speeds in the injection plane, while the flux-weighted injection emphasizes the high speeds as shown in Figure 2. The CTRW model provides a good estimate for the peak and the tail behavior at all distances from the control plane. It overestimates early arrivals at control planes close to the inlet. This is due to the fact, that only a few fractures connect from the inlet to the control

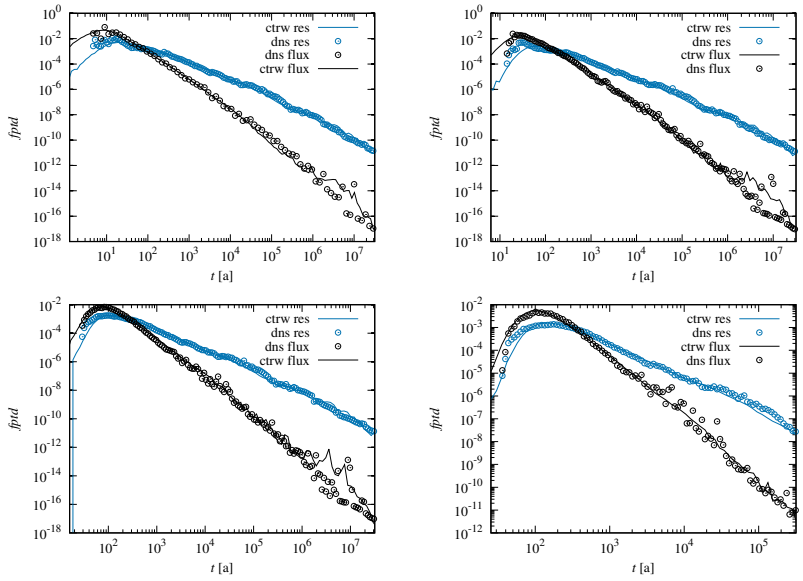

Figure 3: Advective transport: Breakthrough curves at control planes located at (top left to bottom right) $x_c = 250, 500, 750$ and 1000 m for (blue) uniform and (black) flux-weighted injection. The symbols denote the direct numerical simulations, the lines denote the CTRW model data.

planes close to the inlet, while the CTRW model simulates access to to the full spectrum of fracture velocities. Thus, the prediction of early arrivals improves with distance from the control plane because particle are able to sample a larger part of the velocity spectrum.

Figure 4 shows breakthrough curves for the two different injection modes, (left) uniform and (right) flux-weighted. We show both the data from the direct numerical simulations and the CTRW model at 250 and 1000 m. We also include the breakthrough curves at (dotted lines) $x = 5000$ and (dash-dotted lines) 10^4 m which are extrapolations based on the CTRW model. We can observe two different power-law regimes that correspond to the power-laws identified for the speed distributions in Figure 2. Furthermore, we see that the tails of the breakthrough curves for the uniform injection essentially collapse. This can be traced back to the fact that the tail behavior here is dominated by the large transition times the particles experience during the first step. For the flux-

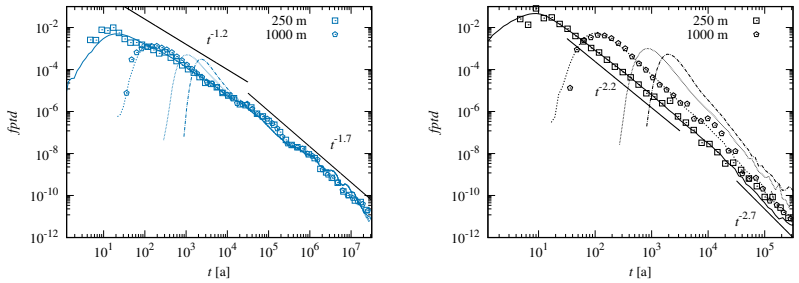

Figure 4: Advective transport: Breakthrough curves obtained from the CTRW model at (solid line) $x_c = 250$, (dashed) 1000, (dotted) 5000 and (dash-dotted) 10^4 m for (left) uniform and (right) flux-weighted injection. The symbols denote the breakthrough data at $x_c = 250$ m and 1000 m from the direct numerical simulations.

weighted injection, the tails show the same power-law behavior, but seem to collapse at much larger times than for the uniform injection. They are due to repeated sampling from the low velocity end of the speed distribution.

5.2. Advective transport under matrix diffusion

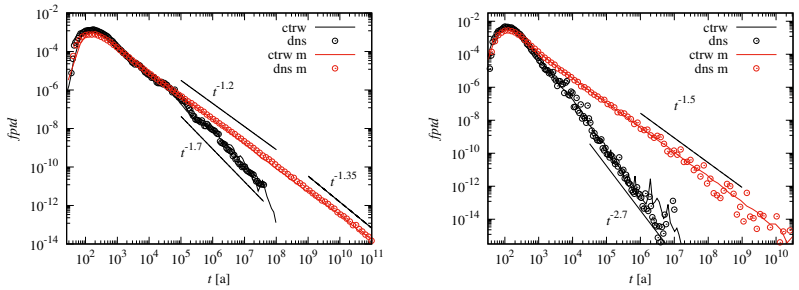

Figure 5: Breakthrough curves for (black) purely advective transport and (red) with matrix diffusion for (left) uniform and (right) flux-weighted initial conditions at $x_c = 1000$ m.

Figure 5 compares breakthrough curves a the control plane at $x = 1000$ m for pure advection and under matrix diffusion for uniform (left) and flux-weighted (right) initial distributions. It clearly illustrates the increased tailing due to solute retention in the matrix. Again, the tailing is stronger for the case of uniform injection. In this case, strong retention in the source zone due to low flow speeds competes with retention due to matrix diffusion, which leads to

the power-law behavior as $t^{-1-\alpha/2}$ as discussed in Section 3.3, where α is the exponent that characterizes the power-law regimes for the velocity distributions shown in Figure 2. The breakthrough curves for the flux-weighted injection are dominated by matrix diffusion and show the characteristic $t^{-3/2}$ scaling.

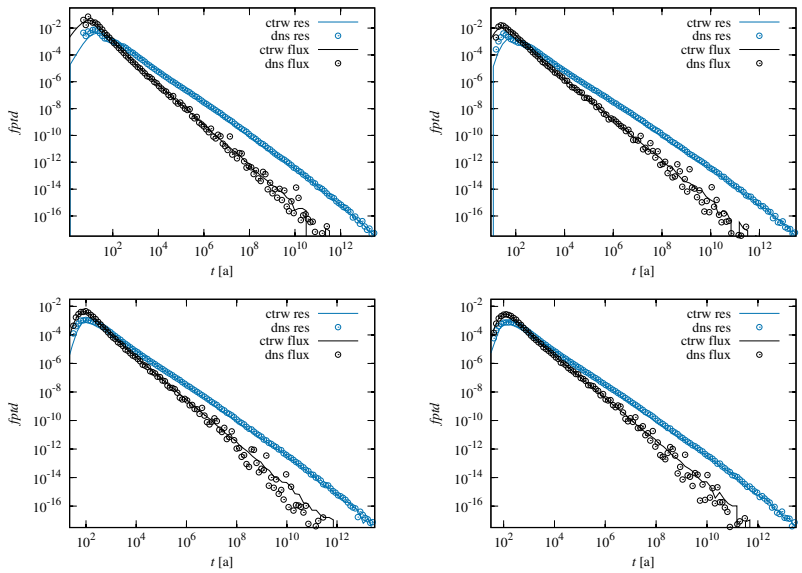

Figure 6: Advective transport under matrix diffusion: Breakthrough curves at control planes located at (top left to bottom right) $x_c = 250, 500, 750$ and 1000 m for (blue) uniform and (black) flux-weighted injection. The symbols denote the direct numerical simulations, the lines denote the CTRW model data.

Figure 6 shows breakthrough curves at different control planes for uniform and flux-weighted initial conditions under matrix diffusion. The CTRW model provides good estimates for peak and the tail behavior at all distances from the injection plane. Early arrivals are overestimated at control planes close to the injection plane. As for the purely advective case, this can be traced back to the fact that only a few dominant fractures connect the injection and control plane while the CTRW model simulates availability of the full fracture spectrum. Thus, the CTRW estimates for early arrival times improve with distance from the inlet plane as more fractures are sampled.

Figure 7 shows breakthrough at distances $x = 250, 1000, 5000$ m and 10000

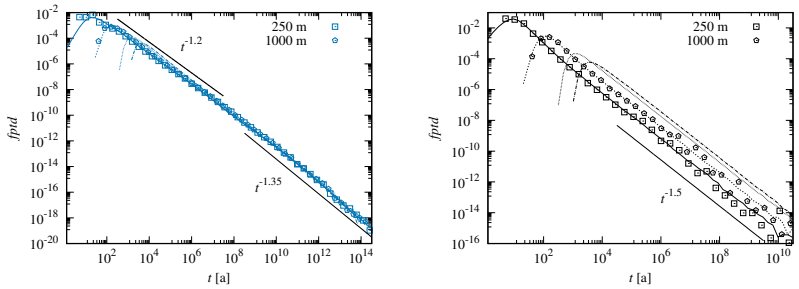

Figure 7: Advective transport under matrix diffusion: Breakthrough curves obtained from the CTRW model at (solid line) $x_c = 250$, (dashed) 1000, (dotted) 5000 and (dash-dotted) 10^4 m for (left) uniform and (right) flux-weighted injection. The symbols denote the breakthrough data at $x_c = 250$ m and 1000 m from the direct numerical simulations.

m from the inlet plane. The breakthrough curves at (dotted lines) $x = 5000$ and (dash-dotted lines) 10^4 m are extrapolations based on the CTRW model. The strong retention due to low flow speeds in the source zone combined with matrix diffusion dominates the tail behavior for uniform injection. The tails of the breakthrough curves essentially collapse. For the flux-weighted injection the tails show the same scalings, but separate, again due to the repeated sampling of low velocities and retention in the matrix along a particle path.

6. Conclusions

We investigate and upscale the combined effect of flow heterogeneity and matrix diffusion on conservative transport in three-dimensional fracture networks under different initial solute distributions. Direct numerical simulations for flow and particle transport give insight into the advective and diffusive transport mechanisms and the impact of heterogeneity and retention due to matrix diffusion on solute breakthrough curves at different observation planes. In order to probe the impact of the initial solute distribution, we consider resident/uniform particle injections over the inlet plane as well as flux-weighted injection. We observe significant power-law tailing in the solute travel time distribution due to advective heterogeneity and a broad velocity distribution within the networks.

This tailing is amplified under resident injection. In this scenario, the solute is distributed equally across all velocities within the inlet plane, which leads to stronger retention at the initial plane due to low speeds than for the flux-weighted injection condition. In the presence of matrix diffusion, the breakthrough tailing is amplified both for the flux-weighted and resident injection conditions. For the flux-weighted injection, we observe the characteristic $t^{-3/2}$ late time scaling. In the case of resident injection, we observe a different scaling. In this case, the interaction of strong retention due to low flow speeds along with immobilization in the matrix leads to a different scaling behavior.

We quantify these behaviors using an upscaled CTRW approach that accounts for advective heterogeneity and retention in the matrix, conditioned on the initial solute data. Velocity variability along each pathline is modeled as a stationary Markov process where the velocity changes at equidistant positions along the path. Specifically, we map the particle speed onto a Gaussian random variable which evolves according to an Ornstein-Uhlenbeck process. The proces is parameterized by the Lagrangian speed distribution and correlation distance, which in principle can be obtained from the Eulerian speed PDF and characteristic fracture scale. Advective transition times are obtained kinematically from the constant transition distance and speed. This approach captures the impact of flow variability and injection condition on breakthrough curve tailing. We use a compound Poisson process to model retention due to diffusion into the matrix blocks, which means trapping events occur at a constant rate along a particle pathline. The trapping time distribution is governed by an inverse Gaussian distribution. Thus, trapping times are sampled from an inverse Gaussian random variable where the trapping rate is given by the diffusion coefficient in the matrix, matrix porosity, and the effective fracture aperture. This upscaled approach captures the combined effect of flow heterogeneity, and matrix diffusion on solute transport and breakthrough at control planes at variable distances from the inlet and gives analytical predictions for the long time scalings. The model relates the intermediate scalings of the breakthrough curves to advective heterogeneity, and the distribution of particle and thus flow speeds. The latter

depends on the network properties such as aperture distribution and correlation between fracture length and aperture [42]. In this sense, the advective breakthrough curve scalings reflect and change with the network structure. The characteristic $t^{-3/2}$ scaling, however, is due to the fracture-matrix exchange and independent of the medium structure. The upscaled model provides insights into the mechanism and the complex interactions between advective and diffusive mass transfer mechanisms. Furthermore it provides a computationally efficient tool to extrapolate transport to distances and times difficult to reach using direct numerical simulations.

The upscaled model is parameterized by the distribution of Lagrangian speeds, which in principle can be inferred from the Eulerian speed distribution, a flow property, by tortuosity and by the velocity correlation scale, which depend on the network and flow properties. The relation between geometric and hydraulic network properties and these characteristics is an outstanding question that needs to be answered to bridge the gap between medium properties and flow and transport behaviors. The proposed upscaled approach captures the main physical transport processes that dominate conservative tracer transport. It shows that particle motion in a complex fracture network can be by quantified by an upscaled CTRW model based on a Markov process that is parameterized by point statistics of speed, and a single correlation scale, as well as a Poissonian trapping process for fracture-matrix echange. The proposed mathematical formulation for fracture-matrix interaction can be used also to model linear kinetic adsorption of a solute to the solid matrix. Furthermore, the model can be generalized to chemical reactions of single species and between particles by combining the CTRW model with suitable rules for particle survival and interactions.

Acknowledgments

JDH thanks the Department of Energy Basic Energy Sciences program (LANLE3W1), and the Spent Fuel and Waste Science and Technology Cam-

paign, Office of Nuclear Energy, of the U.S. Department of Energy under contract number Los Alamos National Laboratory is operated by Triad National Security, LLC, for the National Nuclear Security Administration of U.S. Department of Energy (Contract No. 89233218CNA000001). This work was prepared as an account of work sponsored by an agency of the United States Government. The views and opinions of authors expressed herein do not necessarily state or reflect those of the United States Government or any agency thereof, its contractors or subcontractors. MD gratefully acknowledges the support of the Spanish Ministry of Science and Innovation through the project HydroPore (PID2019-106887GB-C31). Los Alamos National Laboratory unclassified release number: LA-UR-21-22994.

Appendix A. TDRW for Matrix Diffusion

For a pulse injection into a single uniform fracture surrounded by an infinite matrix, [22] derived an analytical solution considering only advection within the fracture. The probability density function of travel times exiting the fracture may be obtained from their solution as:

$$P(t|t_f) = \begin{cases} \dfrac{at_f}{\sqrt{\pi}(t-t_f)^{\frac{3}{2}}} \exp\left(\dfrac{-a^2{t_f}^2}{(t-t_f)}\right) & \text{if} \quad t > t_f \\ 0 & \text{if} \quad t \leq t_f \end{cases} \tag{A.1}$$

where t_f is the advective travel time through a fracture, and

$$a = \frac{\phi\sqrt{D_m}}{b} \ . \tag{A.2}$$

Here, ϕ is the matrix porosity, D_m is the matrix diffusivity, and b is the fracture aperture, which can vary between fractures but not within them using this formulation. From (A.1), the cumulative density function (CDF) for the travel time distribution in a single fracture that accounting for both advection and matrix diffusion is:

$$F(t) = \text{erfc}\left(\frac{at_f}{\sqrt{t-t_f}}\right) \ . \tag{A.3}$$

Particle tracking simulations provide the advective travel time of a particle in a fracture (t_f). The time retained in the matrix can be obtained using the the inverse CDF method

$$t_d = \left(\frac{at_f}{\text{erfc}^{-1}(\xi)}\right)^2 \ , \tag{A.4}$$

where, erfc is the complementary error function and ξ is a random number drawn from the uniform distribution between 0 and 1. The total travel time to pass through a fracture (t) is the sum of t_f and t_d.

Appendix B. Trapping rate

The relation (19) can be understood by considering the travel time distribution over a single fracture predicted by the Eulerian matrix diffusion formulation.

It is given in Laplace space by [22, 21]

$$f^*(\lambda, \tau_f) = \exp[-\lambda\tau_f - (2\phi\tau_f/a)\lambda\varphi^*(\lambda)] \tag{B.1}$$

By setting $\varphi^*(\lambda) = \sqrt{D_m/\lambda}$, we obtain

$$f^*(\lambda, \tau_f) = \exp[-\lambda\tau_f - \tau_f(2\phi\sqrt{D_m}/a)\sqrt{\lambda}] \tag{B.2}$$

Note that the factor of 2 comes from the symmetry of matrix diffusion across both fracture-matrix interfaces.

From the CTRW model, we obtain in Laplace space

$$f^*(\lambda, \tau_f) = \exp(-\lambda\tau_f - \gamma[1 - p_m^*(\lambda)]) \tag{B.3}$$

The Laplace transform of the trapping time pdf is

$$p_m^*(\lambda) = \exp(-\sqrt{\lambda\epsilon^2/D_m}) \approx 1 - \sqrt{\lambda\epsilon^2/D_m}. \tag{B.4}$$

Thus, the arrival time distribution over a single fracture can be written in the limit $\epsilon \ll 1$ as

$$f^*(\lambda, \tau_f) = \exp(-\lambda\tau_f - (\gamma\epsilon/\sqrt{D_m}\sqrt{\lambda}) \tag{B.5}$$

Comparison between (B.2) and (B.5) gives

$$2\phi\sqrt{D_m}/a = \gamma\epsilon/\sqrt{D_m} \tag{B.6}$$

and thus

$$\gamma = \frac{2\phi D_m}{\epsilon a} \tag{B.7}$$

Appendix C. Scaling of breakthrough curves

The Laplace transform of $\psi_a(t)$ can be expanded as

$$\psi_a^*(\lambda) = 1 - \bar{\tau}\lambda + a(\lambda\tau_0)^\beta, \tag{C.1}$$

where $\bar{\tau}$ is the mean advective transition time, τ_0 a characteristic time scale, and a a constant that depends on the particular form of $\psi_a(t)$. The Laplace

transform of $\psi_0(t)$ for $1 < \beta < 2$ is analogous. For $0 < \beta < 1$, the Laplace transform of $\psi_0(t)$ is given by

$$\psi_0^*(\lambda) = 1 - c(\lambda\tau_0)^\beta, \tag{C.2}$$

where c is a constant. Furthermore, we note that the trapping time distribution $\psi_f(t)$ has the Laplace transform

$$\psi_f^*(\lambda) = \exp(-\sqrt{\lambda\epsilon^2/D_m}) \approx 1 - \sqrt{\lambda\epsilon^2/D_m}. \tag{C.3}$$

We first consider the case $\psi_0(t) \approx \psi_a(t)$ such that expression (26) simplifies to

$$f^*(\lambda, x) = \psi_a^*(\lambda + \gamma[1 - \psi_f^*(\lambda)])^{n_c}, \tag{C.4}$$

Using expressions (C.1) and (C.3) in Equation (C.4), we can write

$$f^*(\lambda, x) = \exp\left(n_c \ln\left[1 - \bar{\tau}\lambda - \bar{\tau}\gamma\sqrt{\lambda\epsilon^2/D_m}) + a\tau_0^\beta(\lambda + \gamma\sqrt{\lambda\epsilon^2/D_m})^\beta\right]\right) \tag{C.5}$$

Expanding the logarithm gives

$$f^*(\lambda, x) = \exp\left[-\bar{t}_c\left(\lambda + \sqrt{\lambda/\tau_e}\right) + a\bar{t}_c\bar{\tau}^{-1}\tau_0^\beta\left(\lambda + \sqrt{\lambda/\tau_e}\right)^\beta\right] \tag{C.6}$$

where we defined $\tau_e = \gamma^2\epsilon^2/D$ and $\bar{t}_c = n_c\bar{\tau}$. The scale τ_e marks the time at which particles have spent in average the same time in the fracture and the matrix. For $\lambda\tau_e \gg 1$, we can expand

$$f^*(\lambda, x) \approx 1 - \bar{t}_c\lambda + a\bar{t}_c\bar{\tau}^{-1}(\tau_0\lambda)^\beta \tag{C.7}$$

and thus $f(t, x) \propto t^{-1-\beta}$ for $\bar{t}_c \ll t \ll \tau_e$. For times $t \gg \tau_e$, retention in the matrix dominates the breakthrough curves. For $\lambda\tau_e \ll 1$, we can expand

$$f^*(\lambda, x) \approx 1 - \bar{t}_c\sqrt{\lambda/\tau_e}, \tag{C.8}$$

and thus $f(t, x) \propto t^{-3/2}$.

We now consider the case that $\psi_0(t) \sim t^{-1-\alpha}$ where $0 < \alpha < 1$ and $\psi_a(t) \sim t^{-2-\alpha}$. Thus, we can expand $f^*(\lambda)$ as

$$f^*(\lambda, x) = \exp\left[-c\tau_0^\alpha \left(\lambda + \sqrt{\lambda/\tau_e}\right)^\alpha\right] \times \exp\left[-\bar{t}_c \left(\lambda + \sqrt{\lambda/\tau_e}\right) + a\bar{t}_c\bar{\tau}^{-1}\tau_0^{\alpha+1}\left(\lambda + \sqrt{\lambda/\tau_e}\right)^{\alpha+1}\right] \tag{C.9}$$

where we set $(n_c - 1)\bar{\tau} \approx \bar{t}_c$. For $\lambda\tau_0 \ll 1$, we can expand

$$f^*(\lambda, x) = 1 - c\tau_0^\alpha \left(\lambda + \sqrt{\lambda/\tau_e}\right)^\alpha - \bar{t}_c \left(\lambda + \sqrt{\lambda/\tau_e}\right) + a\bar{t}_c\bar{\tau}^{-1}\tau_0^{\alpha+1}\left(\lambda + \sqrt{\lambda/\tau_e}\right)^{\alpha+1} \tag{C.10}$$

For $\lambda\tau_e \gg 1$ we further obtain

$$f^*(\lambda, x) = 1 - c\left(\lambda\tau_0\right)^\alpha - \bar{t}_c\lambda + a\bar{t}_c\bar{\tau}^{-1}\left(\lambda\tau_0\right)^{\alpha+1} \tag{C.11}$$

For $t \gg \bar{t}_c$, this means $\lambda\bar{t}_c \ll 1$, we have in leading order

$$f^*(\lambda, x) = 1 - c\left(\lambda\tau_0\right)^\alpha, \tag{C.12}$$

which implies that $f(t) \sim t^{-1-\alpha}$. Similarly, for $\lambda\tau_e \ll 1$, we can expand

$$f^*(\lambda, x) = 1 - c\tau_0^\alpha \left(\lambda/\tau_e\right)^{\alpha/2} \tag{C.13}$$

which implies $f(t) \sim t^{-1-\alpha/2}$ for $t \gg \tau_e$.

Appendix D. Effective Aperture

Figure D.8 compares the DFN BTCs including matrix diffusion using the actual fracture hydraulic apertures that vary between fractures (blue squares) and using the effective hydraulic apertures (black circles) at the outlet plane $x_1 = 1000$ m. The left subfigure shows that BTCS for resident injection and the right subfigure shows the results for flux-weighted. There is a slight deviation between the curves at the initial breakthrough but the scaling in the tails of the distributions are the same.

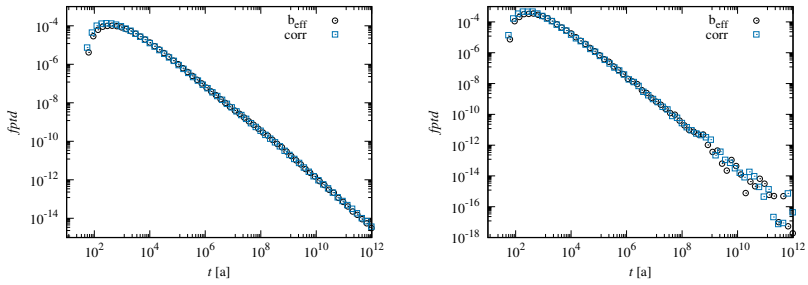

Figure D.8: Comparison of DFN particle tracking that includes matrix diffusion. (left) Resident/Uniform Injection (right) Flux-weighted Injection. The blue squares show the BTC where the TDRW for matrix diffusion uses the actual hydraulic apertures, which vary between fractures, and the black circles show the TDRW results using a single effective apertures.

References

[1] B. Berkowitz, Characterizing flow and transport in fractured geological media: A review, Adv. Water Resour. 25 (8-12) (2002) 861–884.

[2] E. Bonnet, O. Bour, N. E. Odling, P. Davy, I. Main, P. Cowie, B. Berkowitz, Scaling of fracture systems in geological media, Rev. Geophys. 39 (3) (2001) 347–383.

[3] National Research Council, Rock fractures and fluid flow: contemporary understanding and applications, National Academy Press, 1996.

[4] The National Academies of Sciences, Engineering, and Medicine, Characterization, modeling, monitoring, and remediation of fractured rock, National Academies Press, 2021.

[5] S. Neuman, Trends, prospects and challenges in quantifying flow and transport through fractured rocks, Hydrogeol. J. 13 (1) (2005) 124–147.

[6] C.-F. Tsang, I. Neretnieks, Flow channeling in heterogeneous fractured rocks, Rev. Geophys. 36 (2) (1998) 275–298.

[7] C.-F. Tsang, Coupled hydromechanical-thermochemical processes in rock fractures, Rev. Geophys. 29 (4) (1991) 537–551.

[8] V. Cvetkovic, J. Selroos, H. Cheng, Transport of reactive tracers in rock fractures, J. Fluid Mech. 378 (1999) 335–356.

[9] J.-R. de Dreuzy, Y. Méheust, G. Pichot, Influence of fracture scale heterogeneity on the flow properties of three-dimensional discrete fracture networks, J. Geophys. Res.-Sol. Ea. 117 (B11) (2012).

[10] Y. Edery, S. Geiger, B. Berkowitz, Structural controls on anomalous transport in fractured porous rock, Water Rescour. Res. 52 (7) (2016) 5634–5643.

[11] P. Grindrod, M. Impey, Channeling and fickian dispersion in fractal simulated porous media, Water Resour. Res. 29 (12) (1993) 4077–4089.

[12] J. D. Hyman, M. Dentz, A. Hagberg, P. Kang, Emergence of stable laws for first passage times in three-dimensional random fracture networks, Phys. Rev. Lett. 123 (24) (2019) 248501.

[13] J. D. Hyman, Flow channeling in fracture networks: Characterizing the effect of density on preferential flow path formation, Water Resources Research 56 (9) (2020) e2020WR027986.

[14] P. K. Kang, M. Dentz, T. Le Borgne, R. Juanes, Spatial Markov model of anomalous transport through random lattice networks, Phys. Rev. Lett. 107 (2011) 180602.

[15] S. Painter, V. Cvetkovic, J.-O. Selroos, Power-law velocity distributions in fracture networks: Numerical evidence and implications for tracer transport, Geophys. Res. Lett. 29 (14) (2002).

[16] M. W. Becker, A. M. Shapiro, Tracer transport in fractured crystalline rock: Evidence of nondiffusive breakthrough tailing, Water Resour. Res. 36 (7) (2000) 1677–1686.

[17] J. Carrera, X. Sánchez-Vila, I. Benet, A. Medina, G. Galarza, J. Guimerà, On matrix diffusion: formulations, solution methods and qualitative effects, Hydrogeol. J. 6 (1) (1998) 178–190.

[18] I. Neretnieks, Diffusion in the rock matrix: An important factor in radionuclide retardation?, J. Geophys. Res. Sol. Ea. 85 (B8) (1980) 4379–4397.

[19] G. Grisak, J.-F. Pickens, Solute transport through fractured media: 1. the effect of matrix diffusion, Water Resour. Res. 16 (4) (1980) 719–730.

[20] R. Haggerty, S. W. Fleming, L. C. Meigs, S. A. McKenna, Tracer tests in a fractured dolomite: 2. analysis of mass transfer in single-well injection-withdrawal tests, Water Resour. Res. 37 (5) (2001) 1129–1142.

[21] J. D. Hyman, H. Rajaram, S. Srinivasan, N. Makedonska, S. Karra, H. Viswanathan, G. Srinivasan, Matrix diffusion in fractured media: New insights into power law scaling of breakthrough curves, Geophys. Res. Lett. 46 (23) (2019) 13785–13795. arXiv:https://agupubs.onlinelibrary.wiley.com/doi/pdf/10.1029/2019GL085454, doi:10.1029/2019GL085454.
URL https://agupubs.onlinelibrary.wiley.com/doi/abs/10.1029/2019GL085454

[22] P. Małoszewski, A. Zuber, On the theory of tracer experiments in fissured rocks with a porous matrix, Journal of Hydrology 79 (3-4) (1985) 333–358.

[23] P. Maloszewski, A. Zuber, Tracer experiments in fractured rocks: matrix diffusion and the validity of models, Water Resour. Res. 29 (8) (1993) 2723–2735.

[24] L. C. Meigs, R. L. Beauheim, Tracer tests in a fractured dolomite: 1. experimental design and observed tracer recoveries, Water Resour. Res. 37 (5) (2001) 1113–1128.

[25] A. M. Shapiro, Effective matrix diffusion in kilometer-scale transport in fractured crystalline rock, Water Resour. Res. 37 (3) (2001) 507–522.

[26] Q. Zhou, H.-H. Liu, F. J. Molz, Y. Zhang, G. S. Bodvarsson, Field-scale effective matrix diffusion coefficient for fractured rock: Results from literature survey, J. Contam. Hydrol. 93 (1-4) (2007) 161–187.

[27] A. Kreft, A. Zuber, On the physical meaning of the dispersion equation and its solutions for different initial and boundary conditions, Chemical Engineering Science 33 (11) (1978) 1471–1480. doi:10.1016/0009-2509(78)85196-3.

[28] G. Demmy, S. Berglund, W. Graham, Injection mode implications for solute transport in porous media: Analysis in a stochastic Lagrangian framework, Water Resour. Res. 35 (7) (1999) 1965–1973.

[29] A. Frampton, V. Cvetkovic, Significance of injection modes and heterogeneity on spatial and temporal dispersion of advecting particles in two-dimensional discrete fracture networks, Adv. Water Resour. 32 (5) (2009) 649–658.

[30] A. Frampton, V. Cvetkovic, Numerical and analytical modeling of advective travel times in realistic three-dimensional fracture networks, Water Resour. Res. 47 (2) (2011).

[31] H. Gotovac, V. Cvetkovic, R. Andricevic, Flow and travel time statistics in highly heterogeneous porous media, Water Resour. Res. 45 (7) (2009).

[32] H. Gotovac, V. Cvetkovic, R. Andricevic, Significance of higher moments for complete characterization of the travel time probability density function in heterogeneous porous media using the maximum entropy principle, Water Resour. Res. 46 (5) (2010).

[33] I. Janković, A. Fiori, Analysis of the impact of injection mode in transport through strongly heterogeneous aquifers, Adv. Water Resour. 33 (10) (2010) 1199–1205.

[34] J. D. Hyman, S. L. Painter, H. Viswanathan, N. Makedonska, S. Karra, Influence of injection mode on transport properties in kilometer-scale three-dimensional discrete fracture networks, Water Resour. Res. 51 (9) (2015) 7289–7308.

[35] P. K. Kang, M. Dentz, T. Le Borgne, S. Lee, R. Juanes, Anomalous transport in disordered fracture networks: spatial Markov model for dispersion with variable injection modes, Adv. Water Resour. 106 (2017) 80–94.

[36] P. K. Kang, J. D. Hyman, W. S. Han, M. Dentz, Anomalous transport in three-dimensional discrete fracture networks: Interplay between aperture heterogeneity and injection modes, Water Resources Research 56 (11) (2020) e2020WR027378.

[37] J. Vanderborght, D. Mallants, J. Feyen, Solute transport in a heterogeneous soil for boundary and initial conditions: Evaluation of first-order approximations, Water Resour. Res. 34 (12) (1998) 3255–3270.

[38] A. Puyguiraud, P. Gouze, M. Dentz, Upscaling of anomalous pore-scale dispersion, Transport in Porous Media 128 (2) (2019) 837–855. doi:10.1007/s11242-019-01273-3.
URL https://doi.org/10.1007/s11242-019-01273-3

[39] A. Comolli, V. Hakoun, M. Dentz, Mechanisms, upscaling, and prediction of anomalous dispersion in heterogeneous porous media, Water Resources Research 55 (10) (2019) 8197–8222. doi:10.1029/2019wr024919.
URL https://doi.org/10.1029/2019wr024919

[40] M. Dentz, P. Kang, A. Comolli, T. Le Borgne, D. R. Lester, Continuous time random walks for the evolution of lagrangian velocities, Phys. Rev. Fluids 1 (7) (2016) 074004.

[41] A. Comolli, M. Dentz, Anomalous dispersion in correlated porous media: a coupled continuous time random walk approach, Eur. Phys. J. B 90 (9) (2017) 166.

[42] J. D. Hyman, M. Dentz, A. Hagberg, P. Kang, Linking structural and transport properties in three-dimensional fracture networks, J. Geophys. Res.-Sol. Ea. (2019).

[43] B. Berkowitz, H. Scher, On characterization of anomalous dispersion in porous and fractured media, Water Resour. Res. 31 (6) (1995) 1461–1466.

[44] J. H. Cushman, D. O'Malley, Fickian dispersion is anomalous, J. Hydrol. 531 (2015) 161–167.

[45] Y. Tsang, Study of alternative tracer tests in characterizing transport in fractured rocks, Geophys. Res. Lett. 22 (11) (1995) 1421–1424.

[46] J. Hadermann, W. Heer, The grimsel (switzerland) migration experiment: integrating field experiments, laboratory investigations and modelling, J. Contam. Hydrol. 21 (1-4) (1996) 87–100.

[47] R. Haggerty, S. A. McKenna, L. C. Meigs, On the late-time behavior of tracer test breakthrough curves, Water Resour. Res. 36 (12) (2000) 3467–3479.

[48] S. Geiger, A. Cortis, J. Birkholzer, Upscaling solute transport in naturally fractured porous media with the continuous time random walk method, Water Resour. Res. 46 (12) (2010).

[49] A. Comolli, J. J. Hidalgo, C. Moussey, M. Dentz, Non-fickian transport under heterogeneous advection and mobile-immobile mass transfer, Transport in Porous Media 115 (2) (2016) 265–289.

[50] A. Comolli, J. J. Hidalgo, C. Moussey, M. Dentz, Non-fickian transport under heterogeneous advection and mobile-immobile mass transfer, Transport in Porous Media 115 (2) (2016) 265–289.

[51] I. Berre, F. Doster, E. Keilegavlen, Flow in fractured porous media: A review of conceptual models and discretization approaches, Transp. Porous Media 130 (1) (2019) 215–236.

[52] J. Bodin, G. Porel, F. Delay, Simulation of solute transport in discrete fracture networks using the time domain random walk method, Earth Planet. Sc. Lett. 208 (3-4) (2003) 297–304.

[53] F. Delay, J. Bodin, Time domain random walk method to simulate transport by advection-dispersion and matrix diffusion in fracture networks, Geophys. Res. Lett. 28 (21) (2001) 4051–4054.

[54] S. L. Painter, V. Cvetkovic, J. Mancillas, O. Pensado, Time domain particle tracking methods for simulating transport with retention and first-order transformation, Water Resour. Res. 44 (1) (2008).

[55] B. Berkowitz, A. Cortis, M. Dentz, H. Scher, Modeling non-fickian transport in geological formations as a continuous time random walk, Rev. Geophys. 44 (2) (2006).

[56] D. A. Benson, S. W. Wheatcraft, M. M. Meerschaert, Application of a fractional advection-dispersion equation, Water Rescour. Res. 36 (6) (2000) 1403–1412.

[57] M. Dentz, P. Gouze, A. Russian, J. Dweik, F. Delay, Diffusion and trapping in heterogeneous media: An inhomogeneous continuous time random walk approach, Adv. Water Resour. 49 (2012) 13–22.

[58] S. Fomin, T. Hashida, V. Chugunov, A. Kuznetsov, A borehole temperature during drilling in a fractured rock formation, International Journal of Heat and Mass Transfer 48 (2) (2005) 385–394.

[59] S. A. Fomin, V. A. Chugunov, T. Hashida, Non-fickian mass transport in fractured porous media, Adv. Water Resour. 34 (2) (2011) 205–214.

[60] B. Berkowitz, C. Naumann, L. Smith, Mass transfer at fracture intersections: An evaluation of mixing models, Water Resour. Res. 30 (6) (1994) 1765–1773. doi:10.1029/94WR00432.
URL https://agupubs.onlinelibrary.wiley.com/doi/abs/10.1029/94WR00432

[61] H. W. Stockman, C. Li, J. L. Wilson, A lattice-gas and lattice boltzmann study of mixing at continuous fracture junctions: Importance of boundary conditions, Geophys. Res. Lett. 24 (12) (1997) 1515–1518.

[62] Y. J. Park, K. K. Lee, B. Berkowitz, Effects of junction transfer characteristics on transport in fracture networks, Water Resour. Res. 37 (4) (2001) 909–923. doi:10.1029/2000WR900365.

[63] Y. Park, K. Lee, G. Kosakowski, B. Berkowitz, Transport behavior in three-dimensional fracture intersections, Water Resour. Res. 39 (8) (2003). arXiv:https://agupubs.onlinelibrary.wiley.com/doi/pdf/10.1029/2002WR001801, doi:10.1029/2002WR001801.
URL https://agupubs.onlinelibrary.wiley.com/doi/abs/10.1029/2002WR001801

[64] P. K. Kang, M. Dentz, T. Le Borgne, R. Juanes, Anomalous transport on regular fracture networks: Impact of conductivity heterogeneity and mixing at fracture intersections, Phys. Rev. E 92 (2) (2015) 022148.

[65] T. Sherman, J. D. Hyman, D. Bolster, N. Makedonska, G. Srinivasan, Characterizing the impact of particle behavior at fracture intersections in three-dimensional discrete fracture networks, Phys. Rev. E (2018).

[66] R. Haggerty, S. M. Gorelick, Multiple-rate mass transfer for modeling diffusion and surface reactions in media with pore-scale heterogeneity, Water Resour. Res. 31 (10) (1995) 2383–2400.

[67] V. L. Morales, M. Dentz, M. Willmann, M. Holzner, Stochastic dynamics of intermittent pore-scale particle motion in three-dimensional porous media: Experiments and theory, Geophysical Research Letters 44 (18) (2017) 9361–9371.

[68] V. Hakoun, A. Comolli, M. Dentz, Upscaling and prediction of lagrangian velocity dynamics in heterogeneous porous media, Water Resour. Res. 55 (2019) 10.1029/2018WR023810.

[69] A. Puyguiraud, P. Gouze, M. Dentz, Stochastic dynamics of lagrangian pore-scale velocities in three-dimensional porous media, Water Resources

Research 55 (2) (2019) 1196–1217. doi:10.1029/2018wr023702.
URL https://doi.org/10.1029/2018wr023702

[70] R. Benke, S. Painter, Modeling conservative tracer transport in fracture networks with a hybrid approach based on the boltzmann transport equation, Water Resour. Res. (39) (2003) 1324. doi:10.1029/2003WR001966,.

[71] T. Le Borgne, M. Dentz, J. Carrera, Spatial Markov processes for modeling lagrangian particle dynamics in heterogeneous porous media, Phys. Rev. E 78 (2008) 041110.

[72] T. Le Borgne, M. Dentz, J. Carrera, A Lagrangian statistical model for transport in highly heterogeneous velocity fields, Phys. Rev. Lett. 101 (2008) 090601.

[73] J. L. Doob, The brownian movement and stochastic equations, Annals of Mathematics (1942) 351–369.

[74] G. Margolin, M. Dentz, B. Berkowitz, Continuous time random walk and multirate mass transfer modeling of sorption, Chem. Phys. 295 (2003) 71–80.

[75] D. A. Benson, M. M. Meerschaert, A simple and efficient random walk solution of multi-rate mobile/immobile mass transport equations, Adv. Wat. Res. 32 (4) (2009) 532–539.

[76] A. Russian, M. Dentz, P. Gouze, Time domain random walks for hydrodynamic transport in heterogeneous media, Water Resources Research (2016).

[77] G. H. Weiss, Aspects and Applications of the Random Walk, Elsevier North-Holland, 1994.

[78] S. Redner, A guide to first-passage processes, Ca, 2001.

[79] J. D. Hyman, S. Karra, N. Makedonska, C. W. Gable, S. L. Painter, H. S. Viswanathan, dfnWorks: A discrete fracture network framework for modeling subsurface flow and transport, Comput. Geosci. 84 (2015) 10–19.

[80] A. T. Wood, Simulation of the von Mises Fisher distribution, Commun. Stat. Simulat. 23 (1) (1994) 157–164.

[81] K. Klint, P. Gravesen, A. Rosenbom, C. Laroche, L. Trenty, P. Lethiez, F. Sanchez, L. Molinelli, C. Tsakiroglou, Multi-scale characterization of fractured rocks used as a means for the realistic simulation of pollutant migration pathways in contaminated sites: a case study, Water Air Soil Poll. 4 (4-5) (2004) 201–214.

[82] J. D. Hyman, J. Jiménez-Martínez, Dispersion and mixing in three-dimensional discrete fracture networks: Nonlinear interplay between structural and hydraulic heterogeneity, Water Rescour. Res. 54 (5) 3243–3258.

[83] J. De Dreuzy, P. Davy, O. Bour, Percolation threshold of 3d random ellipses with widely-scattered distributions of eccentricity and size, Phys. Rev. E 62 (5) (2000) 5948–5952.

[84] B. Berkowitz, I. Balberg, Percolation theory and its application to groundwater hydrology, Water Resour. Res 29 (4) (1993) 775–794.

[85] O. Bour, P. Davy, Connectivity of random fault networks following a power law fault length distribution, Water Resour. Res. 33 (7) (1997) 1567–1583.

[86] O. Bour, P. Davy, On the connectivity of three-dimensional fault networks, Water Resour. Res. 34 (10) (1998) 2611–2622.

[87] M. Sahimi, Applications Of Percolation Theory, CRC Press, 1994.

[88] J. D. Hyman, C. W. Gable, S. L. Painter, N. Makedonska, Conforming Delaunay triangulation of stochastically generated three dimensional discrete fracture networks: A feature rejection algorithm for meshing strategy, SIAM J. Sci. Comput. 36 (4) (2014) A1871–A1894.

[89] Svensk Kärnbränslehantering AB, Data report for the safety assessment SR-site (TR-10-52), Tech. rep., Svensk Kärnbränslehantering AB (2010).

[90] N. Makedonska, J. D. D. Hyman, S. Karra, S. L. Painter, C. W. W. Gable, H. S. Viswanathan, Evaluating the effect of internal aperture variability on transport in kilometer scale discrete fracture networks, Adv. Water Resour. 94 (2016) 486–497.

[91] A. Frampton, J. D. Hyman, L. Zou, Advective transport in discrete fracture networks with connected and disconnected textures representing internal aperture variability, Water Resour. Res. 55 (7) (2019) 5487–5501.

[92] R. W. Zimmerman, G. S. Bodvarsson, Hydraulic conductivity of rock fractures, Transport Porous Med. 23 (1) (1996) 1–30.

[93] N. Makedonska, S. L. Painter, Q. M. Bui, C. W. Gable, S. Karra, Particle tracking approach for transport in three-dimensional discrete fracture networks, Computat. Geosci. (2015) 1–15.

[94] S. L. Painter, C. W. Gable, S. Kelkar, Pathline tracing on fully unstructured control-volume grids, Computat. Geosci. 16 (4) (2012) 1125–1134.

[95] J. D. Hyman, G. Aldrich, H. Viswanathan, N. Makedonska, S. Karra, Fracture size and transmissivity correlations: Implications for transport simulations in sparse three-dimensional discrete fracture networks following a truncated power law distribution of fracture size, Water Rescour. Res. 52 (8) (2016) 6472–6489. doi:10.1002/2016WR018806.
URL http://dx.doi.org/10.1002/2016WR018806

[96] B. Ghanbarian, A. G. Hunt, R. P. Ewing, M. Sahimi, Tortuosity in porous media: a critical review, Soil science society of America journal 77 (5) (2013) 1461–1477.

[97] A. Koponen, M. Kataja, J. Timonen, Tortuous flow in porous media, Phys. Rev. E 54 (1) (1996) 406.